ChemPubSoc
Europe

SPECIAL
ISSUE

Hydrogen Adsorption

An *In-Situ* Neutron Diffraction and DFT Study of Hydrogen Adsorption in a Sodalite-Type Metal–Organic Framework, Cu-BTTri

Mehrdad Asgari,[a] Rocio Semino,[b,c] Pascal Schouwink,[a] Ilia Kochetygov,[a] Olga Trukhina,[a] Jacob D. Tarver,[d,e] Safak Bulut,[a] Shuliang Yang,[a] Craig M. Brown,[d] Michele Ceriotti,[b] and Wendy L. Queen*[a]

Abstract: Herein we present a detailed study of the hydrogen adsorption properties of Cu-BTTri, a robust crystalline metal–organic framework containing open metal-coordination sites. Diffraction techniques, carried out on the activated framework, reveal a structure that is different from what was previously reported. Further, combining standard hydrogen adsorption measurements with *in-situ* neutron diffraction techniques provides molecular level insight into the hydrogen adsorption process. The diffraction experiments unveil the location of four

D_2 adsorption sites in Cu-BTTri and shed light on the structural features that promote hydrogen adsorption in this material. Density functional theory (DFT), used to predict the location and strength of binding sites, corroborate the experimental findings. By decomposing binding energies in different sites in various energetic contributions, we show that van der Waals interactions play a crucial role, suggesting a possible route to enhancing the binding energy around open metal coordination sites.

Introduction

Metal–organic frameworks (MOFs), a class of porous, crystalline materials, have received intense attention over the last few decades in a variety of fields coupled to gas storage,[1] gas and liquid separations,[2] catalysis,[3] sensing,[4] drug delivery,[5] etc. Among these applications, gas storage has been intensely studied in MOFs;[6] this is largely owed to their unprecedented internal surface areas and pore volumes, combined with the ease of decorating internal surface area with high densities of strong adsorption sites.[7] These attractive features result in high capacities for the capture of a variety of small guest molecules such as hydrogen.[8] When compared to other porous adsorbents, MOFS can offer higher storage capacities,[9] and in some cases boast hydrogen storage densities that exceed what can be achieved through pure compression.[8b,10] While more than

70,000 MOF structures have been reported in literature to date,[11] few of these have been experimentally screened to determine their applicability in hydrogen storage. As such, studies focused on providing knowledge of how the MOF structure influences storage properties are needed. Studies of this kind not only deepen our chemical understanding of adsorption phenomena,[12] but will hopefully promote the development of computational methods able to rapidly and accurately predict the performance of existing and hypothetical materials towards hydrogen gas storage.[13]

One family of MOFs which has shown promising performance for hydrogen storage is the M-BTT (BTT³⁻ = 1,3,5-benzenetristetrazolate where M = Cr, Mn, Fe, Co, Ni, Cu, Cd) series of frameworks.[6,14] This framework family can be substituted with a variety of metals and ligands (BTT³⁻ vs BTTri³⁻ = 1,3,5-benzenetristriazolate or BTP³⁻ = 1,3,5-benzenetrispyrazolate), thus altering the chemical environment inside the MOF pore all while keeping the same structural motif.[15] Further, upon solvent removal, many of these materials exhibit open-metal coordination sites, a structural feature known to increase the surface packing density of hydrogen,[16] and give rise to high isosteric heats of hydrogen adsorption (Q_{st}).[6,14a,17] The latter is required to enhance adsorption capacities at higher temperature, which is desirable for storage on-board vehicles. Given this, herein we report *in-situ* neutron diffraction experiments,[17a,18] which are used to unveil the intimate details of hydrogen adsorption in a highly stable, crystalline MOF, known as Cu-BTTri. In this work we also report the correct structure for the activated Cu-BTTri framework, and location of four D_2 adsorption sites within the gas dosed material, for the first time. In addition, the experi-

[a] *Institute of Chemical Sciences and Engineering,*
   École Polytechnique Fédérale de Lausanne (EPFL),
   CH-1051 Sion, Switzerland
   E-mail: wendy.queen@epfl.ch
   https://isic.epfl.ch/valais
[b] *Institute of Materials, Ecole Polytechnique Fédérale de Lausanne,*
   1015 Lausanne, Switzerland
[c] *Institut Charles Gerhardt Montpellier UMR 5253 CNRS,*
   Université de Montpellier,
   Place E. Bataillon, 34095 Montpellier Cedex 05, France
[d] *National Institute of Standards and Technology,*
   Center for Neutron Research,
   Gaithersburg, Maryland, 20899, USA
[e] *National Renewable Energy Laboratory,*
   Golden, Colorado 80401, USA
   Supporting information and ORCID(s) from the author(s) for this article are available on the WWW under https://doi.org/10.1002/ejic.201801253.

mental data is used to validate density functional theory (DFT) methods, used to predict the location and binding energy of the guest hydrogen species. A good agreement with the experiment implies that this theoretical approach can be applied to simulations of similar systems, thus potentially helping lay the basis for the rapid computational screening of hydrogen adsorption properties of both existing and hypothetical MOF structures in the future.

Results and Discussion

Characterization of the Cu-BTTri Framework

The H_3BTTri ligand and corresponding Cu-BTTri framework were synthesized using reported procedures that were slightly modified (see the Supporting Information). A scanning electron microscope (SEM) was used to assess the size and morphology of the crystallites, Figure S1. The octahedral shape is consistent with the cubic crystal system reported for this material. However, the single crystal size, which is well below 5 μm, inhibits standard single crystal diffraction studies. Due to this limitation, no experimental report of the single crystal structure of Cu-BTTri can be found in the literature. In the original report of Cu-BTTri,[15a] the powder X-ray diffraction data was compared to the simulated powder pattern obtained from its ligand substituted counterpart, Cu-BTT[14b] and assumed to have the following chemical formula: $H_3[(Cu_4Cl)_3(BTTri)_8]$.[15a] In order to check this, neutron powder diffraction data was first collected on the desolvated Cu-BTTri structure, and Rietveld analysis was carried out using the previously reported composition as a starting point. However, this previously reported structure,[15a] shown in Figure S2, did not provide a satisfying fit to the experimental neutron diffraction data obtained in this study. As such, the occupancies of the charge balancing chlorine anions were varied. Interestingly, a good fit could only be achieved by removing Cl⁻ anions from the center of the $[Cu_4Cl]^{7-}$ clusters giving rise to a neutral framework with the following composition: $Cu_3(BTTri)_2$. (Figure S4) To corroborate this finding, the sample was characterized by EDX analysis, which shows no chlorine (Figure S3, Table S1) further supporting the new Cl⁻ free structural model, Figure 1. Cu-BTTri crystallizes in a cubic *Fm-3c* space group (no. 226) and features square $[Cu_4]^{8+}$ clusters that are interlinked by triangular $[BTTri]^{3-}$ ligands to form a sodalite-type framework with a 3-dimensional pore network. The triazole groups of the ligand show rotational disorder resulting in refined partial occupancies of carbon and nitrogen on positions 3 and 5 of the triazolate rings (Table S1). It is noted that this structure was further confirmed via Rietveld analysis carried out on synchrotron X-ray diffraction data also collected on an activated sample of Cu-BTTri. Due to the minimal difference in the X-ray atomic scattering factor for C and N, rotational disorder on the triazole group was neglected. Additionally, hydrogen atoms were excluded during refinement of the structural model. The resulting fit (Figure S5) is satisfactory and additionally confirms the absence of any chlorine species in the activated framework (Figure S6 and Table S2).
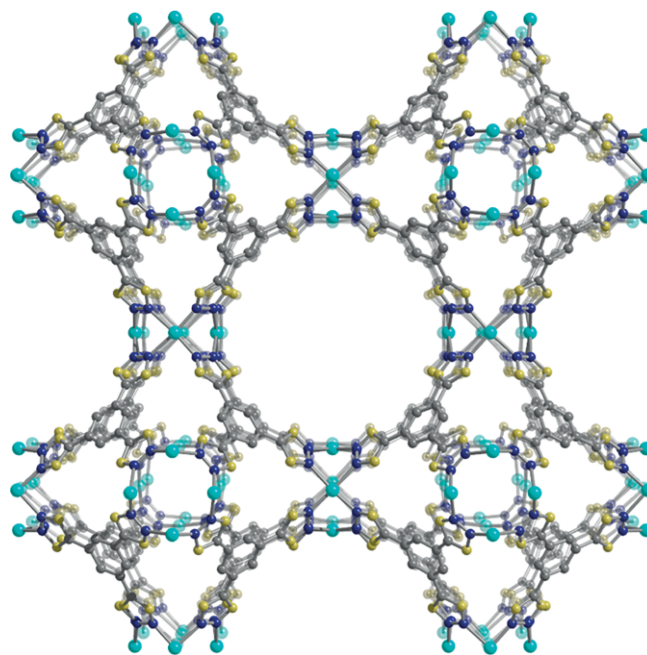
Figure 1. A ball and stick model of the Cu-BTTri structure obtained from Rietveld analysis of powder neutron diffraction data. Cu, N, and C atoms are represented by cyan, blue, and gray spheres, respectively. Yellow spheres represent sites mixed with both C and N. Hydrogen atoms are excluded for clarity.

Surface area and pore volume analysis was carried out on the activated sample via N_2 adsorption isotherms measured at 77 K (Figure S7). The resulting BET surface area and pore volume for this sample are 1950 m²/g and 0.8 cm³/g, respectively. These values are slightly higher than those obtained from the ligand substituted counterpart, Cu-BTT, which were reported to be 1760 m²/g and 0.7 cm³/g, respectively. Unlike Cu-BTTri, the Cu-BTT framework, has extra charge-balancing cations in its framework and Cl⁻ anions centered in the face of the copper cluster. The material has the following chemical formula: $Cu_6[(Cu_4Cl)_3(BTT)_8]Cl_3$. The absence of extra Cu^{2+} and Cl⁻ ions in the Cu-BTTri structure allows the pores to become more accessible and hence will likely alter the performance of this material in various host–guest chemistries.

Hydrogen Adsorption Properties

The low-pressure hydrogen adsorption isotherms were collected for Cu-BTTri at variable temperatures in order to evaluate hydrogen uptake, Figure 2a. Further, the isosteric heat of hydrogen adsorption was extracted from the data obtained at 140 K and 159 K using the Clausius-Clapeyron equation, Figure 2b. A relatively steep slope in the adsorption isotherm for hydrogen is indicative of the presence of strongly polarizing open Cu^{2+} sites. We have compared the low-pressure hydrogen adsorption for Cu-BTTri (measured at 77 K) to its ligand substituted counterpart, Cu-BTT, and see that hydrogen adsorption at low pressures is lower in Cu-BTTri than Cu-BTT (Figure S9). Considering that low-pressure hydrogen adsorption is dictated strongly by the potential energy landscape on the internal

ChemPubSoc
Europe

EurJIC
European Journal
of Inorganic Chemistry

Full Paper

framework surface,[19] the origin of this difference can often be determined via structural analysis.[20] It was hypothesized that the lower H_2 adsorption observed in Cu-BTTri likely originates from the absence of the extra Cu^{2+} cations and Cl^- anions observed in Cu-BTT, or the weaker Lewis acidity of Cu^{2+}, which results from the higher pKa of the $BTTri^{3-}$ ligand. However, the initial isosteric heat of adsorption (Q_{st}) for Cu-BTTri, Figure 2b, is $\approx$ 10.5 kJ/mol, a value that is slightly higher than the one previously reported for Cu-BTT, $\approx$ 9.5 kJ/mol.[6] This indicates that changing the ligand does not strongly influence the binding energy of the first adsorption site.[6] Also, the geometry of the cluster coupled with the structural differences of the framework raises the zero coverage isosteric heat of Cu-BTTri with respect to another Cu^{2+} containing MOF known as Cu-BTC (BTC= benzene-1,3,5-tricarboxylate), which has a paddlewheel-like cluster and a moderate zero coverage isosteric heat of hydrogen adsorption of $\approx$ 6.6 kJ/mol.[21] A similar trend was reported for Cr-BTT and Cr-BTC, with Cr-BTT showing a higher Q_{st}.[6]
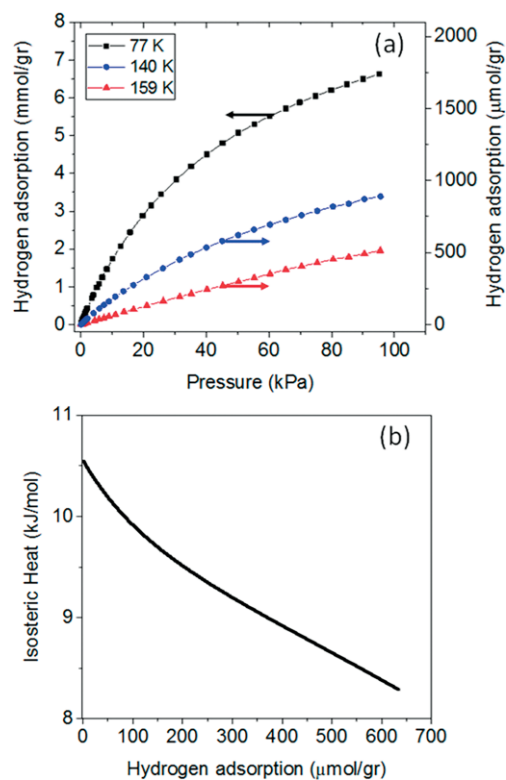
Figure 2. (a) Hydrogen adsorption isotherms in Cu-BTTri collected at 77, 140, and 159 K. (b) Enthalpy of adsorption of H_2 in Cu-BTTri, extracted by the Clausius-Clapeyron equation.

D_2 Binding Sites

Following refinement of the structural model associated with the activated material, the sample was dosed with 0.36 and 3.11 D_2 per Cu^{2+}, and neutron powder diffraction data were subsequently collected at 10 K. Rietveld analysis followed by subsequent Fourier difference analysis allowed determination of the location of the adsorbed D_2 molecules. The D_2 molecules

were modelled as single atoms due to quantum mechanical rotations that make the molecules almost spherical.[22] Fractional atomic coordinates, occupancies, and isotropic displacement parameters of the refined structures are shown in Tables S4 and S5.

From these data, four adsorption sites were identified with the two of them only being present at the higher loading. The locations of these four adsorption sites inside the structure are shown in Figure 3. The site with the highest occupancy [0.13(1) and 0.47(1) D_2 at the loading of 0.36 D_2 per Cu^{2+} and 3.11 D_2 per Cu^{2+}, respectively] is presumed to be the primary adsorption site, and is located at the open Cu^{2+} cation, Figure 3. This site is disordered between two D_2 molecules produced by the mirror plane. The vicinity of the disordered D_2 molecules with the distance of 0.74(9) Å yields in the maximum possible occupancy of 0.5 for the D_2 molecules in this adsorption site, which means that the primary adsorption site is almost fully occupied at 3.11 D_2 per Cu^{2+} loading. The location of $D_2(I)$ confirms our initial assumption that the high initial isosteric heat results from relatively strong interaction between the metal node and D_2. The Cu^{2+}–$D_2(I)$ distance is 2.73(4) Å, which is significantly longer than the value observed for Cu^{2+}–$D_2(I)$ in Cu-BTT or Cu-BTC, 2.47 Å and 2.4 Å, respectively.[14b] The longer Cu–$D_2(I)$ distance likely arises due to the higher electron donating effect of the BTTri ligand compared to BTT,[23] making the Cu^{2+} nodes in Cu-BTTri weaker Lewis acids.[15d] Also, DFT calculations (see Table 1 and Supporting Information) were used to predict the location of the primary adsorption site, $D_2(I)$, which resulted in a distance of 2.65 Å from the Cu^{2+}. Considering the standard deviation for the experimental data, the difference between DFT and experiment is considered to be negligible.
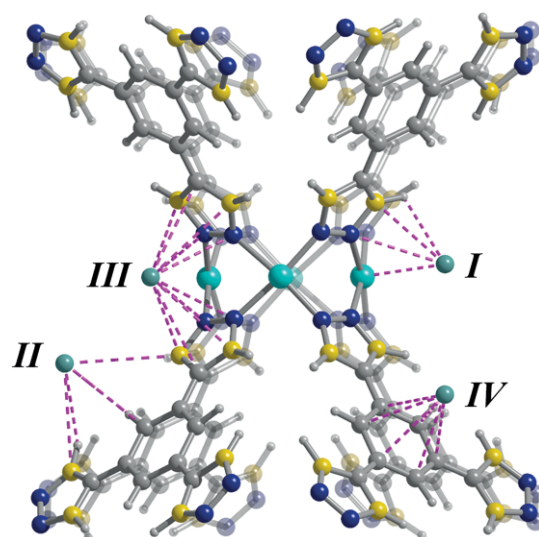
Figure 3. A ball and stick model of the Cu-BTTri framework dosed with 3.11 D_2/Cu^{2+}. The Cu, C, N, and H are denoted as cyan, gray, blue, and white spheres, respectively. Yellow spheres represent mixed sites containing both C and N. The pink dotted lines represent nearest neighbor interactions.

Despite the significantly longer Cu^{2+}–$D_2(I)$ distances observed in Cu-BTTri over Cu-BTT, its zero-coverage isosteric heat

ChemPubSoc
Europe

EurJIC
European Journal
of Inorganic Chemistry

Full Paper

Table 1. Experimental and computed data for D_2 adsorption sites in Cu-BTTri framework.

	Overall Q_{st} (kJ/mol)	Site I −H_b (kJ/mol)	Cu–D(H)	D(H)–N	Site II −H_b (kJ/mol)	D(H)–H	Site III −H_b (kJ/mol)	D(H)–N	Site IV −H_b (kJ/mol)	D–benzene
Experimental	10.5	–	2.73(4)	3.34 (5)	–	2.67(9)	–	3.33(4)	-	≈ 3 Å
DFT	-	10.0	2.65	3.14	3.0	2.87	4.9	3.1	3.0	≈ 3 Å

Q_{st}: zero-coverage isosteric heat of adsorption-H_b: computed enthalpy of hydrogen adsorption. The distances are listed in Å. Values in parentheses indicate one standard deviation.

(10.5 kJ/mol) is slightly higher than that of Cu-BTT (9.5 kJ/mol). This anomaly is confirmed by DFT calculations (Table 1). To better understand the aforementioned differences in Q_{st}, additional secondary interactions between the D_2(I) molecule and the framework must be considered. There are two additional host–guest interactions in Cu-BTTri observed between D_2(I) and the framework. The first and more relevant one is the hydrogen–hydrogen interaction between the hydrogen of the triazole ring and D_2(I) [D_2(I)•••H–C = 2.6(4) Å]. This type of van der Waals interaction was previously observed in MOFs,[20a,24] and should not be confused with dihydrogen bonding, a form of hydrogen bonding with a hydridic hydrogen that plays the role of the base atom.[25] The hydrogen–hydrogen interaction seen in Cu-BTTri, cannot exist in Cu-BTT due to extra nitrogen atom on the tetrazole ring.[14b] It is thought that this strong, secondary interaction is likely responsible for the aforementioned disorder around the D_2(I) site, which could pull the molecule off the mirror plane in Cu-BTTri. (Figure S12) It is noted that this disorder is expectedly not observed for Cu-BTT. The second interaction to be considered is the van der Waals interaction between D_2(I) and the nitrogen atoms of the triazole ring (Figure 3). The distances between D_2(I) and the nitrogen lies within the range of 3.3–3.7 Å, which is reminiscent of weak van der Waals interactions.[26] For Cu-BTTri, the D_2(I)–N interaction is stronger than in Cu-BTT because the triazole nitrogen are stronger electron donors.[23] Therefore, although it is true that the open Cu^{2+} has a major overall contribution to the affinity of the D_2(I) molecules to the framework, the two aforementioned secondary interactions likely compensate for the slightly weaker Lewis acidity of the metal ion in Cu-BTTri giving rise to an overall higher Q_{st}.

The second adsorption site is found between the hydrogen of the benzene ring [D_2(II)•••H–C = 2.67(9) Å] and those of two neighboring triazole rings {[D_2(II)•••H–C = 2.8(1) Å] and [D_2(II)•••H–C = 3.0(1) Å]}. The nature of this type of hydrogen–hydrogen interaction is similar to that of the primary adsorption site. In addition, this site is further stabilized by van der Waals interactions between D_2(II) and the benzene ring [D_2(II)•••H–C = 3.44(6) Å] as well as the nitrogen atoms of two neighboring triazole rings {[D_2(II)•••N = 3.44(6) Å] and [D_2(II)•••N = 3.73(5) Å]}. Moreover, the short D_2–D_2 distances [D_2(II)•••D_2(I) = 2.76(8) Å] imply that the secondary site is likely stabilized by the primary adsorption site. The occupancies of D_2(II) goes from 0.04(1) to 0.45(1) at loadings of 0.36 D_2/Cu^{2+} and 3.11 D_2 per Cu^{2+}. It is noted that the secondary adsorption site previously observed in of Cu-BTT is found directly above the Cl^- in the $[Cu_4Cl]^{7+}$ cluster (Figure S13). The lack of this anion inhibits population

of this site in Cu-BTTri (Figure 3). It is likely that the absence of this relatively strong binding site also lends to its lower hydrogen uptake (Figure S9).

The third adsorption site appears in a pocket located between two neighboring triazole rings, with distances that range from [D_2(III)•••N = 3.33(4) Å], [D_2(III)•••N = 3.36(3) Å], [D_2(III)•••N/C = 3.47(5) Å], [D_2(III)•••N/C = 3.59(3) Å], and [D_2(III)•••C = 3.62(4) Å]. A similar position has been previously observed for Cu-BTT and Fe-BTT.[14a] This adsorption site is not visible in diffraction data collected at 0.36 D_2/Cu^{2+} loading, but is almost fully occupied at the 3.11 D_2 per Cu^{2+} loading.

The quaternary adsorption site in Cu-BTTri is located in the large pore of the framework facing the benzene rings with an approximate distance of 3 Å from the plane of the benzene rings. This site has an occupancy of 0.19(2) D_2.

It can be concluded that van der Waals interactions play a substantial role in the stabilization of the hydrogen adsorption sites in Cu-BTTri. For gases with large permanent multipoles, such as CO_2, binding energy can often be defined largely by the electrostatic interaction, and hence can vary significantly upon modifying the metal identity for instance.[14c] However, if the metal cluster is kept the same, the interaction energy between CO_2 and the framework do not often vary to a large extent upon varying ligands and pore geometry.[27] For molecules with small permanent multipoles, the multiplicity of the interactions is a governing factor that causes the formation of adsorption sites in particular regions of the host structure. Moreover, secondary van der Waals interactions are often comparable to the electrostatic interaction between the guest and host, and as in this case, could compensate for decreases in Lewis acidity of the metal sites. The presence of multiple weak van der Waals interactions and their influence on adsorption sites has also previously been reported for other gases with no dipole or quadrupole moment, such as xenon and krypton.[28]

The locations of sites II–IV were also studied by means of DFT calculations. The shortest D_2-framework distances obtained computationally and experimentally are shown in Table 1. The DFT methods reveal only slightly elongated distances, up to ≈ 0.2 Å when compared to the experimental results. This work confirms the validity of the chosen computational method in the accurate prediction of secondary binding sites.

In order to gather further insight into the D_2 binding energies PBE-D2 DFT calculations were performed. For this, the position of the nuclei from the bare Cu-BTTri and the D_2 molecule were allowed to relax, while the cell parameters were kept constant. The energy of the resulting relaxed structures was com-

ChemPubSoc
Europe

EurJIC
European Journal
of Inorganic Chemistry

Full Paper

puted by a single point calculation, and the binding energies were then extracted as follows:

$$E_{binding} = E_{Cu\text{-}BTTri+D2} - E_{Cu\text{-}BTTri} - E_{D2}$$

The resulting values are shown in Table 1. Note that even though we present positive values for convention, the DFT results were in fact negative, which indicates the stability of the complex with respect to the Cu-BTTri and D_2 alone. The value obtained for the primary adsorption site, $D_2(I)$, is 10 kJ/mol, and is in excellent agreement with the experimental zero coverage isosteric heat of adsorption, 10.5 kJ/mol. These observations validate the DFT method employed in this study, and in previous studies of Poloni et al,[29] which used the same method to predict the nature of CO_2 binding in the isostructural series of M-BTT MOFs. The overall binding energy for the three secondary sites is smaller than $D_2(I)$, which is consistent with the observations made from the diffraction data, which reveals that site I is predominately occupied first.

The calculated binding energies for sites I–IV are also listed in Table 1. Based on the observed occupancies in the diffraction data, we predict the following trend in binding energies: $D_2(I) > D_2(II) > D_2(III) > D_2(IV)$; however, it is noted that the DFT results imply that $D_2(III) > D_2(II)$. This is likely because the calculations are performed considering one gas molecule and the host, and as a consequence, they only take into account D_2-framework interactions, excluding any intermolecular interactions between neighboring D_2 molecules. As such, it is thought that site II is further stabilized by the primary adsorption site increasing the actual binding energy of $D_2(II)$ compared to that predicted by DFT.

Despite this, the calculated binding energies can also help justify the relatively sharp drop in the isosteric heat of adsorption plotted as a function of D_2 loading, Figure 2b. While an energy difference as small as about 3 kJ/mol is sufficient to cause a sequential occupation of adsorption sites at 10 K, at higher temperatures, where adsorption isotherms are collected, it is likely that multiple sites are simultaneously populated.[14c]

To obtain more detailed insight into the nature of the interactions, we also computed the charge density difference induced by the D_2 binding in each adsorption site. For this, we took the sum of the self-consistent charge densities for the empty Cu-BTTri framework and the isolated D_2 molecule and then subtracted that from the self-consistent charge density for the Cu-BTTri+D_2. Plots for two isosurfaces representing the charge density differences are shown in Figure S14, which shows that in all sites the charge density of the molecule becomes polarized by the interactions with the framework. Furthermore, for $D_2(I)$, the interaction mostly occurs through the polarization of the open metal site, as expected. For $D_2(II)$, the imidazole and phenyl moieties of the framework are both polarized, and for $D_2(III)$ the main component of the density distortion involves the imidazole moiety. Finally, for $D_2(IV)$ the charge density difference reveals a sigma–pi interaction between the molecule and the phenyl ring. These observations corroborate what was discussed above based on the distances obtained by Rietveld analyses. While charge density differences give an indication of the parts of the framework that are most per-

turbed by the interaction with the D_2 molecule, they do not necessarily directly indicate the sign and magnitude of the interactions. Given this, the decomposition of the binding energies into the contribution given by the PBE functional (which includes electrostatics and short-range exchange-correlation effects) and those given by the van der Waals interactions, was additionally computed using the Grimme-D2 method, Table 2.

Table 2. Contributions to the binding energies for all adsorption sites.

Site No.	E_{PBE} (kJ/mol)	$E_{Dispersion\text{-}D2}$ (kJ/mol)
1	-0.490	-9.516
2	-0.064	-2.905
3	-0.185	-4.677
4	1.116	-4.152

Even though the E_{PBE} is the most stabilizing for $D_2(I)$, relative to the other sites, this decomposition suggests that van der Waals interactions are the dominant factors in the D_2-CuBTTri binding and determine both the ordering and the overall magnitude of the binding energies. This observation is consistent with the low quadrupole moment of the D_2 molecule, $\Theta_{zz} = 0.39$,[30] and sheds light into the seemingly counter-intuitive observation that the overall experimental zero coverage isosteric heat of adsorption for Cu-BTTri is slightly larger than that observed for Cu-BTT (10.5 versus 9.5 kJ/mol, respectively) despite that the latter has a stronger Lewis acid site. Interestingly, the other M-BTT frameworks, including Fe-BTT, Cr-BTT and Mn-BTT, also show similarities in the isosteric heat of adsorption for the primary adsorption site, ranging from 10.0 to 11.9 kJ/mol. The small effect of metal substitution on the binding energy of the first adsorption site in the M-BTT family is also indicative of the strong role that the van der Waals interactions play at the primary adsorption site.

Conclusions

In this work, we have demonstrated the importance of using *in-situ* diffraction techniques to gain intimate insight into small molecules binding in MOFs. We have shown an accurate structure for Cu-BTTri, which is a critical element required should computational methods be employed to screen this MOF for targeted applications. We have also identified the location of four D_2 adsorption sites in Cu-BTTri and compared our results to those previously reported for a ligand substituted counterpart, Cu-BTT. We show that the DFT method used in this work successfully models hydrogen adsorption sites with minimal deviation from the experimental results. The validation of this computational approach opens the door to predict the adsorption behavior of existing and even hypothetical MOFs.

The identification of the adsorption sites has provided critical insight into the relative impact that different structural elements have on the observed hydrogen adsorption properties of Cu-BTTri. The roles that the open metal site and other secondary van der Waals interactions, like hydrogen–hydrogen interactions, play in the adsorption properties has been assessed using the results of diffraction experiments, and confirmed computationally by an energy-decomposition analysis. We em-

ChemPubSoc
Europe

EurJIC
European Journal
of Inorganic Chemistry

Full Paper

phasize that the contribution by van der Waals interactions plays a crucial role in determining the binding energy, and the ranking of different sites. This critical insight could lead to methods to enhance H_2 binding energies towards those required for room temperature storage (> 15 kJ/mol).[14d]

Experimental Section

Synthesis of H₃BTTri Ligand: The H_3BTTri ligand has been synthesized according to the reported method in the literature.[15a]

Synthesis of Cu-BTTri: The Cu-BTTri framework has been synthesized according to the reported method in the literature[15a] with minor modifications. 225 mg of H_3BTTri ligand was dissolved in 40 mL of DMF in a 100 mL glass jar with the plastic cap. 383 mg of solid $CuCl_2 \cdot 2H_2O$ was also introduced into the jar. After that, 50 droplets of the five times diluted concentrated HCl and 10 mL of water were added to the solution. Then, the cap was sealed and placed in the oven to be heated at 100 °C for 72 hours. Subsequently, the jar was taken out of the oven and was filtered while hot and then washed 3 times with hot DMF and 3 times with MeOH. Then, the sample was dried to yield between 200–250 mg of the product in the form of a purple powder.

Activation of Cu-BTTri: To do the solvent exchange, the sample was placed in a cellulose thimble and then underwent Soxhlet extraction with methanol for 24 hours. Then, the sample was inserted into the sample tubes, sealed and kept under vacuum for 3 hours. Subsequently, the sample was heated to 180 °C over 3 hours and kept at 180 °C for 16 hours to yield the activated product in a form of brown product.

SEM-EDX characterization: SEM analysis was performed on a FEI Teneo at an accelerating voltage of 1.00 kV and a beam current of 100 pA. SEM images were acquired with an in-column (Trinity) detector. SEM-EDX elemental maps were acquired using a beam current of $\approx$ 400 pA and accelerating voltage of 10 kV.

***In-Situ* Neutron Diffraction Experiments:** High-resolution neutron powder diffraction (NPD) experiments were carried out on the Cu-BTTri sample using BT1 at the National Institute of Standards and Technology (NIST) Center for Neutron Research (NCNR). All measurements were carried out on activated samples of about 0.8 g. At NIST, samples were activated while heating under dynamic vacuum and then transferred into a He purged glove-box, loaded into a vanadium can equipped with a gas loading valve, and sealed using an indium O-ring. NPD data were collected using a Ge(311) monochromator with an in-pile 60 collimator corresponding to a wavelength of 2.0728 Å. The sample was loaded onto a closed cycle refrigerator (CCR) and then data was collected at 10 K. After data collection on the activated framework, D_2 with two different dosing levels of 0.36 D_2/Cu^{2+} and 3.11 D_2/Cu^{2+} were then loaded into the sample cell. To do this, the sample was firstly heated to room temperature and then exposed to a pre-determined amount of gas. Upon reaching an equilibrium pressure at the loading temperature, the sample was then slowly cooled (1 K per minute) to ensure complete adsorption of the D_2 and then data was collected again at 10 K. The collected powder diffraction pattern at reduced temperature has been used for further Rietveld analysis. The Rietveld analysis has been done using Topas 5 software.[31]

***In-Situ* Synchrotron X-ray Experiments:** Bare sample was measured at the Swiss-Norwegian Beamlines (BM31) at the European Synchrotron Radiation Facility (ESRF) in Grenoble, France. A custom built *in-situ* diffraction powder cell, which was mountable on the goniometer, was used for *in-situ* variable temperature synchrotron X-ray diffraction experiments. An oxford cryostream 700 system with the working temperature of 80–500 K has been used to keep the temperature of the sample (the zone covered the X-ray beam width) at the desired temperature. The nozzle of the cryostream was tried to be located close enough so as the precision of the temperature will be guaranteed. Data were collected using a MAR 2D image detector and the wavelength was adjusted to be 0.5008 Å. The azimuthal integration of raw images was performed with the program Bubble. Profile fits (Le Bail analysis) and Rietveld refinements of the powder diffraction patterns were performed using EXPGUI/GSAS.

Rietveld Analysis

All diffraction pattern data were analyzed using the Rietveld method as implemented in Topas 5 (for the case of neutron diffraction experiments) and EXPGUI/GSAS (for the case of synchrotron experiment).[31,32] The activated Cu-BTTri model was refined with most structural and peak profile parameters free to vary. Atomic displacement parameters (ADPs) for atoms with the same identity were constrained to be the same throughout the refinement process. Fourier difference analysis, applied to data obtained from D_2 adsorbed samples, was then employed to locate the adsorbed molecules in the frameworks.

CCDC 1872064 (for model Cu-BTTri with 0.36 D_2 per Cu site; 34.6 D_2 per unit cell), 1872065 (for model Cu-BTTri against synchrotron diffraction data from Figure S5), 1872066 (for model Cu-BTTri with 3.11 D_2 per Cu site; 299 D_2 per unit cell), and 1872067 (for model Cu-BTTri against neutron diffraction data from Figure S4) contain the supplementary crystallographic data for this paper. These data can be obtained free of charge from The Cambridge Crystallographic Data Centre.

Quantum Computational Calculation Methods

Binding energies, structural details and charge distribution were obtained from DFT calculations, under the generalized gradient approximation by Perdew, Burke and Ernzerhof (PBE functional).[33] All calculations were performed by using the PWscf (Plane-Wave Self-Consistent Field) package from the Quantum Espresso[34] suite of codes. We used the following ultrasoft pseudopotentials[35] extracted from http://materialscloud.org/sssp: Cu_pbe_v1.2.uspp.F.UPF, C_pbe_v1.2.uspp.F.UPF, H.pbe-rrkjus_psl.0.1.UPF, and N.pbe.theos.UPF. The former two were generated using Vanderbilt code[36] and the latter two using the "atomic" code by A. Dal Corso.[37] We employed kinetic energy cutoffs for wave functions and charge density and potential of 55 and 660 Ry respectively. All calculations were performed for the Γ point of the Brillouin zone, due to the large size of the MOF (228 atoms in the unit cell). Spin-polarized calculations were performed to take into account the most stable spin state for Cu-BTTri, which was found to be antiferromagnetic. Following previous work[29] where other chemically similar MOFs including Cu-BTT were studied, dispersion corrections were considered under the Grimme-D2 scheme.[38]

We took as a starting point the experimental configuration for Cu-BTTri, and then allowed the structure to relax while keeping the cell parameters fixed to experimental values (tests allowing the cell parameters to change were also carried out and have shown very small changes of 1–3 % in volume). Subsequently, several calculations were set, each of them containing one gas molecule adsorbed in a different site of the MOF. We took as initial configurations those found in the experiment and allowed them to relax, again without changing the cell parameters. Binding energies were computed as

the difference between the energy of the MOF/gas binary complex and the sum of the energies of MOF and gas molecule.

Acknowledgments

Keywords: Metal–organic frameworks · Hydrogen · Neutron diffraction · Density functional calculations

[1] a) J. A. Mason, M. Veenstra, J. R. Long, *Chem. Sci.* **2014**, *5*, 32–51; b) N. L. Rosi, J. Eckert, M. Eddaoudi, D. T. Vodak, J. Kim, M. O'keeffe, O. M. Yaghi, *Science* **2003**, *300*, 1127–1129; c) J. L. Rowsell, O. M. Yaghi, *Angew. Chem. Int. Ed.* **2005**, *44*, 4670–4679; *Angew. Chem.* **2005**, *117*, 4748–4758; d) M. Asgari, W. L. Queen, in *Materials and Processes for CO2 Capture, Conversion, and Sequestration* (Eds.: L. Li, W. Wong-Ng, K. Huang, L. P. Cook), Wiley, **2018**, pp. 1–78; e) G. Férey, C. Serre, T. Devic, G. Maurin, H. Jobic, P. L. Llewellyn, G. De Weireld, A. Vimont, M. Daturi, J.-S. Chang, *Chem. Soc. Rev.* **2011**, *40*, 550–562.

[2] a) J.-R. Li, R. J. Kuppler, H.-C. Zhou, *Chem. Soc. Rev.* **2009**, *38*, 1477–1504; b) B. Van de Voorde, B. Bueken, J. Denayer, D. De Vos, *Chem. Soc. Rev.* **2014**, *43*, 5766–5788; c) I. Kochetygov, S. Bulut, M. Asgari, W. L. Queen, *Dalton Trans.* **2018**, *47*, 10527–10535; d) Y.-X. Tan, Y.-P. He, J. Zhang, *Cryst. Growth Des.* **2012**, *12*, 2468–2471.

[3] a) J. Lee, O. K. Farha, J. Roberts, K. A. Scheidt, S. T. Nguyen, J. T. Hupp, *Chem. Soc. Rev.* **2009**, *38*, 1450–1459; b) A. Corma, H. García, F. Llabrés i Xamena, *Chem. Rev.* **2010**, *110*, 4606–4655.

[4] L. E. Kreno, K. Leong, O. K. Farha, M. Allendorf, R. P. Van Duyne, J. T. Hupp, *Chem. Rev.* **2011**, *111*, 1105–1125.

[5] P. Horcajada, C. Serre, M. Vallet-Regí, M. Sebban, F. Taulelle, G. Férey, *Angew. Chem. Int. Ed.* **2006**, *45*, 5974–6124; *Angew. Chem.* **2006**, *118*, 6120–6124.

[6] E. D. Bloch, W. L. Queen, M. R. Hudson, J. A. Mason, D. J. Xiao, L. J. Murray, R. Flacau, C. M. Brown, J. R. Long, *Angew. Chem. Int. Ed.* **2016**, *55*, 8605–8609; *Angew. Chem.* **2016**, *128*, 8747–8751.

[7] a) G. Férey, *Chem. Soc. Rev.* **2008**, *37*, 191–214; b) Z. Zhang, Z.-Z. Yao, S. Xiang, B. Chen, *Energy Environ. Sci.* **2014**, *7*, 2868–2899; c) Y. Liu, Z. U. Wang, H. C. Zhou, *Greenhouse Gases Sci. Technol.* **2012**, *2*, 239–259.

[8] a) M. P. Suh, H. J. Park, T. K. Prasad, D.-W. Lim, *Chem. Rev.* **2011**, *112*, 782–835; ##111-111## b) M. Dincă, J. R. Long, *Angew. Chem. Int. Ed.* **2008**, *47*, 6766–6779; *Angew. Chem.* **2008**, *120*, 6870.

[9] L. J. Murray, M. Dincă, J. R. Long, *Chem. Soc. Rev.* **2009**, *38*, 1294–1314.

[10] a) H.-C. Zhou, J. R. Long, O. M. Yaghi, *Chem. Rev.* **2012**, *112*, 673–674; b) J. Ren, B. C. North, *J. Technol. Innovations Renewable Energy* **2014**, *3*, 12.

[11] M. Tong, Y. Lan, Q. Yang, C. Zhong, *Green Energy Environment.* **2018**, *3*, 107–119.

[12] J. S. Lee, B. Vlaisavljevich, D. K. Britt, C. M. Brown, M. Haranczyk, J. B. Neaton, B. Smit, J. R. Long, W. L. Queen, *Adv. Mater.* **2015**, *27*, 5785–5796.

[13] a) T. Sagara, J. Klassen, E. Ganz, *J. Chem. Phys.* **2004**, *121*, 12543–12547; b) T. Mueller, G. Ceder, *J. Phys. Chem. B* **2005**, *109*, 17974–17983.

[14] a) K. Sumida, S. Horike, S. S. Kaye, Z. R. Herm, W. L. Queen, C. M. Brown, F. Grandjean, G. J. Long, A. Dailly, J. R. Long, *Chem. Sci.* **2010**, *1*, 184–191; b) M. Dincă, W. S. Han, Y. Liu, A. Dailly, C. M. Brown, J. R. Long, *Angew. Chem. Int. Ed.* **2007**, *46*, 1419–1422; *Angew. Chem.* **2007**, *119*, 1441; c) M. Asgari, S. Jawahery, E. D. Bloch, M. R. Hudson, R. Flacau, B. Vlaisavljevich, J. R. Long, C. M. Brown, W. L. Queen, *Chem. Sci.* **2018**, *9*, 4579–4588; d) M. Dinca, A. Dailly, Y. Liu, C. M. Brown, D. A. Neumann, J. R. Long, *J. Am. Chem. Soc.* **2006**, *128*, 16876–16883.

[15] a) A. Demessence, D. M. D'Alessandro, M. L. Foo, J. R. Long, *J. Am. Chem. Soc.* **2009**, *131*, 8784–8786; b) D. J. Xiao, M. I. Gonzalez, L. E. Darago, K. D. Vogiatzis, E. Haldoupis, L. Gagliardi, J. R. Long, *J. Am. Chem. Soc.* **2016**, *138*, 7161–7170; c) D. A. Reed, D. J. Xiao, M. I. Gonzalez, L. E. Darago, Z. R. Herm, F. Grandjean, J. R. Long, *J. Am. Chem. Soc.* **2016**, *138*, 5594–5602; d) G. C. Shearer, V. Colombo, S. Chavan, E. Albanese, B. Civalleri, A. Maspero, S. Bordiga, *Dalton Trans.* **2013**, *42*, 6450–6458.

[16] Y. Liu, H. Kabbour, C. M. Brown, D. A. Neumann, C. C. Ahn, *Langmuir* **2008**, *24*, 4772–4777.

[17] a) W. L. Queen, E. D. Bloch, C. M. Brown, M. R. Hudson, J. A. Mason, L. J. Murray, A. J. Ramirez-Cuesta, V. K. Peterson, J. R. Long, *Dalton Trans.* **2012**, *41*, 4180–4187; b) D. Gygi, E. D. Bloch, J. A. Mason, M. R. Hudson, M. I. Gonzalez, R. L. Siegelman, T. A. Darwish, W. L. Queen, C. M. Brown, J. R. Long, *Chem. Mater.* **2016**, *28*, 1128–1138; c) S. Yang, L. Peng, E. Oveisi, S. Bulut, D. T. Sun, M. Asgari, O. Trukhina, W. L. Queen, *Chem. Eur. J.* **2018**, *24*, 4234–4238.

[18] a) W. L. Queen, M. R. Hudson, E. D. Bloch, J. A. Mason, M. I. Gonzalez, J. S. Lee, D. Gygi, J. D. Howe, K. Lee, T. A. Darwish, *Chem. Sci.* **2014**, *5*, 4569–4581; b) E. D. Bloch, W. L. Queen, R. Krishna, J. M. Zadrozny, C. M. Brown, J. R. Long, *Science* **2012**, *335*, 1606–1610; c) E. D. Bloch, L. J. Murray, W. L. Queen, S. Chavan, S. N. Maximoff, J. P. Bigi, R. Krishna, V. K. Peterson, F. Grandjean, G. J. Long, *J. Am. Chem. Soc.* **2011**, *133*, 14814–14822.

[19] X. Lin, I. Telepeni, A. J. Blake, A. Dailly, C. M. Brown, J. M. Simmons, M. Zoppi, G. S. Walker, K. M. Thomas, T. J. Mays, *J. Am. Chem. Soc.* **2009**, *131*, 2159–2171.

[20] a) M. Savage, I. Da Silva, M. Johnson, J. H. Carter, R. Newby, M. Suyetin, E. Besley, P. Manuel, S. Rudić, A. N. Fitch, *J. Am. Chem. Soc.* **2016**, *138*, 9119–9127; b) L. Kong, V. R. Cooper, N. Nijem, K. Li, J. Li, Y. J. Chabal, D. C. Langreth, *Phys. Rev. B* **2009**, *79*, 081407.

[21] H. Lee, Y. N. Choi, S. B. Choi, J. Kim, D. Kim, D. H. Jung, Y. S. Park, K. B. Yoon, *J. Phys. Chem. C* **2013**, *117*, 3177–3184.

[22] C. M. Brown, Y. Liu, T. Yildirim, V. K. Peterson, C. J. Kepert, *Nanotechnology* **2009**, *20*, 204025.

[23] J. Catalan, J. Elguero, in *Adv. Heterocycl. Chem. Vol. 41*, Elsevier, **1987**, pp. 187–274.

[24] C. F. Matta, J. Hernández-Trujillo, T. H. Tang, R. F. Bader, *Chem. Eur. J.* **2003**, *9*, 1940–1951.

[25] Y. A. Abramov, L. Brammer, W. T. Klooster, R. M. Bullock, *Inorg. Chem.* **1998**, *37*, 6317–6328.

[26] D. J. Sutor, *J. Chem. Soc. (Resumed)* **1963**, 1105–1110.

[27] a) B. Zheng, J. Bai, J. Duan, L. Wojtas, M. J. Zaworotko, *J. Am. Chem. Soc.* **2011**, *133*, 748–751; b) N. Al-Janabi, P. Hill, L. Torrente-Murciano, A. Garforth, P. Gorgojo, F. Siperstein, X. Fan, *Chem. Eng. J.* **2015**, *281*, 669–677.

[28] a) C. M. Simon, R. Mercado, S. K. Schnell, B. Smit, M. Haranczyk, *Chem. Mater.* **2015**, *27*, 4459–4475; b) M. Witman, S. Ling, S. Jawahery, P. G. Boyd, M. Haranczyk, B. Slater, B. Smit, *J. Am. Chem. Soc.* **2017**, *139*, 5547–5557; c) D. Banerjee, C. M. Simon, A. M. Plonka, R. K. Motkuri, J. Liu, X.

Chen, B. Smit, J. B. Parise, M. Haranczyk, P. K. Thallapally, *Nat. Commun.* **2016**, *7*, ncomms11831.

[29] R. Poloni, K. Lee, R. F. Berger, B. Smit, J. B. Neaton, *J. Phys. Chem. Lett.* **2014**, *5*, 861–865.

[30] I. Mitxelena, M. Piris, *J. Chem. Phys.* **2016**, *144*, 204108.

[31] A. A. Coelho, *J. Appl. Crystallogr.* **2018**, *51*, 210–218. 213 ; b) B. H. Toby, *J. Appl. Crystallogr.* **2001**, *34*, 210–213.

[32] a) A.C. Larson and R.B. Von Dreele, General Structure Analysis System(GSAS). *Report LAUR, Los Alamos National Laboratory.* **2000**, 86-748.

[33] J. P. Perdew, K. Burke, M. Ernzerhof, *Phys. Rev. Lett.* **1996**, *77*, 3865.

[34] P. Giannozzi, S. Baroni, N. Bonini, M. Calandra, R. Car, C. Cavazzoni, D. Ceresoli, G. L. Chiarotti, M. Cococcioni, I. Dabo, *J. Phys. Condens. Matter* **2009**, *21*, 395502.

[35] D. Vanderbilt, *Phys. Rev. B* **1990**, *41*, 7892.

[36] K. F. Garrity, J. W. Bennett, K. M. Rabe, D. Vanderbilt, *Comput. Mater. Sci.* **2014**, *81*, 446–452.

[37] A. Dal Corso, *Comput. Mater. Sci.* **2014**, *95*, 337–350.

[38] S. Grimme, *J. Comput. Chem.* **2006**, *27*, 1787–1799.